ZnxMnO2/PPy nanowires composite as cathode material for aqueous Zinc-ion hybrid supercapacitors

Yujia Xue[1], Jinghao Huo[2], Xin Wang[2], and Yuzhen Zhao[3]

[1]Xi'an Fanyi University
[2]Shaanxi University of Science and Technology
[3]Xijing University

September 02, 2024

Abstract

Over the past decade, the extensive consumption of finite energy resources has caused severe environmental pollution. Meanwhile, the promotion of renewable energy sources is limited by their intermittent and regional nature. Thus, developing effective energy storage and conversion technologies and devices holds considerable importance. Zinc-ion hybrid supercapacitors (ZISCs) merge the beneficial aspects of both supercapacitors and batteries, rendering them an exceptionally promising energy storage method. As an important cathode material for ZISCs, the tunnel structure MnO_2 has poor conductivity and structural stability. Herein, the Zn_xMnO_2/PPy (ZMOP) electrode materials are prepared by hydrothermal method. Doping with Zn^{2+} is used to enhance its structural stability, while adding polypyrrole to improve its conductivity. Therefore, the fabricated ZMOP cathode presents superb specific capacity (0.1 A g^{-1}, 156.4 mAh g^{-1}) and remarkable cycle performance (82.6%, 5000 cycles, 0.2 A g^{-1}). Furthermore, the assembled aqueous ZISCs with ZMOP cathode and PPy-derived porous carbon nanotubes anode obtain a superb capacity of 109 F g^{-1} at 0.1 A g^{-1}. Meanwhile, at a power density of 867 W kg^{-1}, the corresponding energy density can achieve 20 Wh kg^{-1}. And over 5000 cycles at 0.2 A g^{-1}, the ZISCs can exhibit excellent cycle stability (86.4%). This suggests that ZMOP nanowires are potential cathode materials for superior-performance aqueous ZISCs.

1. Introduction

With fast advancements in wearable and portable electronics, the urgent need for a comprehensive array of energy storage solutions with high surface energy and power densities, quick charging-discharging, and stable cycle performance has been raised and is being widely explored.[1-5]

The primary obstacle hampering the practical utilization of zinc ion hybrid supercapacitors (ZISCs) is the scarcity of cathode materials with high reversible capacitance, reliable cycling stability, and suitable operating voltage. Transition metal oxides exhibit excellent electrochemical properties in aqueous solution, including fast discharge kinetics and high multiplicity performance.[6-10]MnO_2 has become a particularly attractive option for ZISCs cathode materials due to its reasonable price, ease of processing, and eco-friendliness.[11] Due to the tunneling and layered structure, MnO_2 can offer ample pathways and active sites for the transport and embedding of various ions, such as Li, Na, K, and Zn ions.[12] Xu et al. assembled the ZISCs with the MnO_2 nanorods anode, AC cathode, and $ZnSO_4$ (2M) electrolyte, and different mass ratios of electrodes were investigated.[13] At the most suitable mass ratio of 2.5:1, the ZISCs could operate with an operating range of 0-2.0 V. The structure and conductivity of MnO_2-based ZISCs need to be improved to gain a commercial market position. Chen et al. studied the pre-intercalation of Zn^{2+} on the carbon cloth with a substantial loading quantity of 12 mg cm^{-2} to grow highly stabilized Zn_xMnO_2 nanowires with tunneling structures, obtaining excellent electrochemical properties.[14] However, the lack of MnO_2 conductivity still affects the cycling stability of ZISCs.[15,16]

In the present work, a new type of ZISCs is assembled using Mn-based cathode and carbon-based anode materials. ZnxMnO_2 (ZMO) nanowires were fabricated by the ordinary hydrothermal method, and investigated the microscopic morphology structure and electrochemical performance of ZMO/PPy (ZMOP). The addition of $Zn(NO_3)_2$ provides a Zn^{2+} ion, which makes the structure of MnO_2 more stable than before. The unique structure of PPy can greatly improve the electrical conductivity and cycle efficiency of Mn-based electrodes. When ZMOP was used as the cathode material of ZISCs, the PPy-derived porous carbon nanotubes (PCNTs) were selected as the anode material to assemble ZMOP//PCNT ZISCs. The insertion-extraction on the positive electrode of ZMOP nanowires and the adsorption-desorption on the PCNTs negative electrode shows excellent electrochemical properties. The assembled ZISCs delivered an outstanding energy density of 37 wh kg^{-1} with a power density of 64 w kg^{-1}, it could maintain a capacity of 86.4% for 5000 cycles at 0.2 Ag^{-1}.

2. Experiment Section

2.1 Materials

Zinc nitrate hexahydrate ($Zn(NO_3)_2{\cdot}6H_2O$) was bought from Tianjin Fengchuan Co., Ltd. Potassium permanganate ($KMnO_4$, [?]99.5%) was obtained from Luoyang Haohua Co., Ltd. Methyl orange ($C_{14}H_{14}N_3SO_3Na$, AR), Pyrrole (C_4H_5N, [?]99%), and Iron chloride hexahydrate ($FeCl_3$*$6H_2O$, AR) were purchased from Shanghai Aladdin Co., Ltd. Commercial sulphuric acid (H_2SO_4) 99.9%, and ethanol were used as received which were purchased from China National Pharmaceutical Group Co., Ltd. All aqueous solutions are formulated with deionized (DI) water, and the chemicals can be used without any further purification.

2.2 The synthesis of electrode material

2.2.1 The preparation of PPy nanotubes

PPy nanotubes were manufactured by the easy template oxidation procedure. 3.75 mM of methyl orange and 25 mM of pyrrole (Py) were added to 150 mL of DI water, and then stirred for 0.5 h (labeled as solution A). The $FeCl_3$*$6H_2O$ (with the same molar amount as Py) was added in 50 mL of DI water (labeled as solution B). Afterward, gradually mix solution B and solution A, stir for 10 min, and then place in a -4 refrigerator to stand for 24 hours. The PPy nanotubes were then filtered multiple times and cleaned with DI water and anhydrous ethanol till the filtered solution was transparent, removing organic and inorganic impurities from the sample. The PPy nanotubes were dried in an oven for 24 hours at a temperature of 60 degC.

2.2.2 ZMOP cathode material

The preparation process of the ZMOP nanowires composite is shown in**Figure1** . Firstly, 0.8848 g $KMnO_4$ and 1.6 g $Zn(NO_3)_2$ are dispersed in 50 mL DI water, then 2 mL 98% H_2SO_4 is added, and solution A is obtained after stirring for 15 min. Then, 20 mg, 40 mg, and 60 mg of PPy were dispersed in 20 mL of DI water to get solution B. Finally, solution B was dispersed in solution A, and after stirring for 30 min, the mixed precursor was moved to the polyvinylidene fluoride lining (100 mL) , and then transferred to the stainless steel autoclave. The sealed autoclave heated for 3.5 h and kept at 140 degC. After cooling to room temperature, clean with DI water, and finally dry in a vacuum oven at 70 degC to successfully obtain ZMOP-x (x indicates different contents (2, 4, 6) of PPy).

2.2.3 PCNTs anode material

The PCNTs were prepared by using the method reported in the literature.[17-19]

2.3 Material Characterization

The morphology of the synthesized materials was investigated by a field emission scanning electron microscope (SEM, Hitachi SU8100, Japan) and a field emission transmission electron microscope (TEM, FEI Tecnai G2 F20 S-TWIN, USA). Meanwhile, the chemical composition ZMOP-x was tested by energy dispersive

spectrometer (EDS). The crystal structure of the as-prepared materials was studied by X-ray diffractometer (XRD, D/max2200PC, Cu Kα radiation = 1.5406 Å, Japan). All data were tested with 2ϑ values ranging from 10° to 70° with 2°/min scan rate. X-ray photoelectron spectroscopy (XPS, ESCALAB 250X, USA) was utilized to ascertain the elemental type and valence states within the samples. The Fourier transform infrared spectroscopy (FTIR) was used to analyze the molecular framework of the materials.

2.4 Electrochemical Measurement

The ZISCs were assembled with ZMOP cathode, PCNTs anode, and $ZnSO_4$ electrolyte. The diaphragm for assembling ZISCs consisted of GF/D Whatman glass fibers. At the same time, the properties of ZMOP//PCNTs ZISCs were evaluated using coin cells operating within the range of 0 to 1.9 V. The preparation procedure for the ZMOP cathode entails the following steps: initially, a mixture of ZMOP-x, polytetrafluoroethylene, and acetylene black of 8:1:1 (in a mass ratio), which is thoroughly ground into an even paste-like consistency. This is then rolled out to create a coating of identical thickness. Next, the coating is dried for 24 h at 60°C and subsequently cut into a round slice with a diameter of 1.6 cm. And then the approximate mass of every piece is about 1.7-1.8 mg cm^{-2}. Cyclic voltammetry (CV) and electrochemical impedance spectroscopy (EIS) assessments were conducted using CHI660E electrochemical workstation (Chenhua, China). The EIS results were gathered over a frequency range from 105 Hz to 0.01 Hz. Galvanostatic charging-discharging (GCD) data were tested by a battery testing system (CT3002A, Land, China). The energy density (E, Wh kg^{-1}) and power density (P, W kg^{-1}) for the ZISCs were calculated using the equations (1)-(2),

$$E=\frac{I\times\int V\,dt}{3.6\times m}(1)$$

$$P=\frac{E}{t}\times 3600\ (2)$$

where I (A) signifies the current during the charging-discharging process, V (V) denotes the voltage, m (g) indicates the mass of the electrodes, and t (s) represents the discharging time, respectively.

3. Results and Discussion

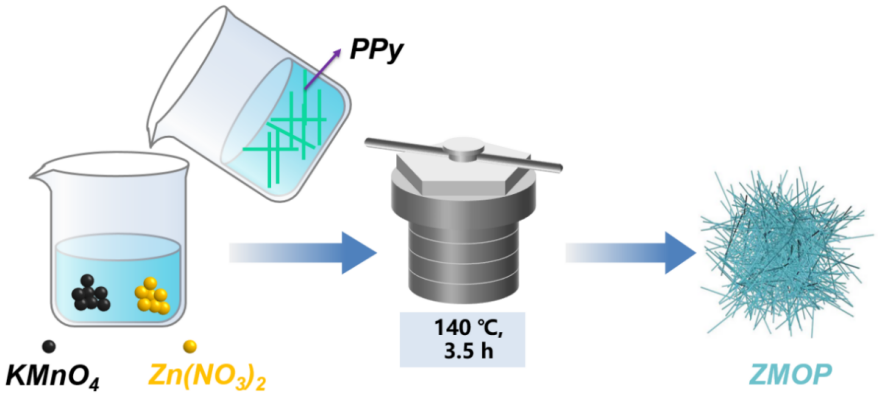

not-yet-known not-yet-known

not-yet-known

unknown

Figure 1. Abridged schematic of the preparation procedure for ZMOP

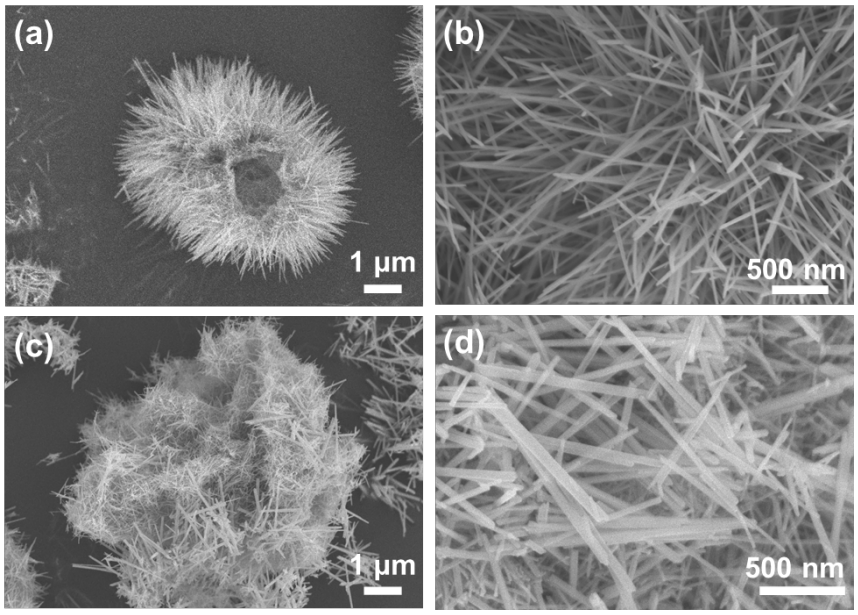

Figure 2. SEM images of (a, b) ZMO; (c, d) ZMOP-4

As shown in **Figure 3b-f** , it is obvious that ZMOP-4 simultaneously contains the elements of Mn, O, N, and Zn, and they are evenly dispersed. The uniform distribution of the N element proves the successful addition of PPy.

To further determine the phase of PPy and ZMOP-x, XRD patterns of the materials were tested and analyzed. In **Figure 4a** , XRD results of ZMO and ZMOP-x nanowires show the diffraction peak corresponds to that of the standard card α-MnO_2 (JCPDS44-0141), reflecting that the doping of a little bit of Zn^{2+}won't influence the original crystal structure of MnO_2. These several main identifying peaks at 12.8, 18.1, 26.8, 37.5, 41.9, 49.8, and 60.3° equivalent to points to the (110), (200), (310), (211), (301), (411), and (521) crystalline planes of α-MnO_2, respectively.[20-22] PPy sample has a distinct broad peak at 25°, which corresponds to the (002) planes of graphite. Hence, The XRD data indicates that the as-prepared PPy exhibits an amorphous structure. In addition, due to the small content of PPy in the ZMOP-x composite, the peak of PPy is not very obvious in the obtained XRD pattern.

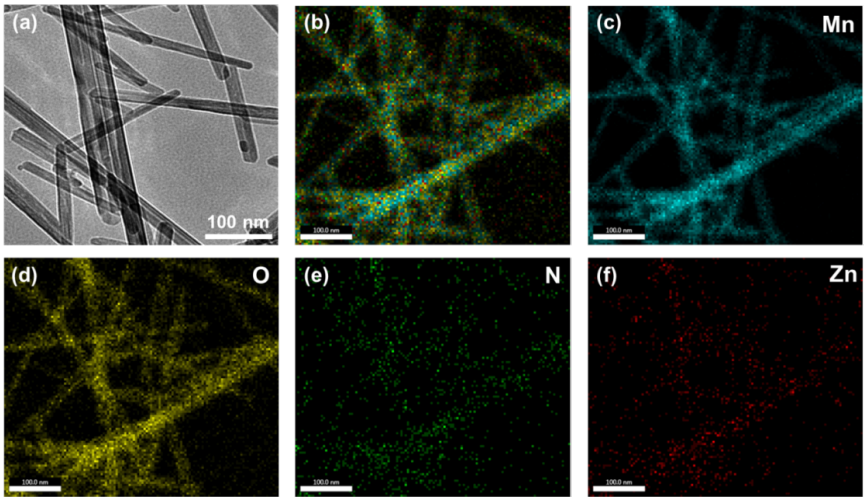

Figure 3. (a) TEM diagram of ZMOP-4; (b-f) Mn, O, N, Zn element distribution diagram of ZMOP-4

In **Figure 4b** , the detailed molecular framework of the ZMOP-x composites was conducted by FTIR. It can be seen that the different amount of PPy mainly affects the peak position of 1120 cm^{-1}. Among them, when there is no or little content of PPy was added, the formation of the peak couldn't be seen at the peak of 1120 cm^{-1}. With the increasing amount of PPy, ZMOP-4, and ZMOP-6 samples have weak peaks at the position of 1120 cm^{-1}, indicating that the C-N tensile vibration strength of these two ratios is relatively high. Further indicating that the appropriate addition of PPy has a favorable impact on the electrode material to promote the transport and diffusion process of Zn^{2+}, and benefits by offering more active points to increase the Zn^{2+} storage.[23,24] In Figure 4b, the peak for the C=C/C-C skeleton vibration is observed at 1630 cm^{-1}, while the C-H in-plane vibration peak appears at 1400 cm^{-1}. And peaks at 978 cm^{-1} are owed to the N-H out-of-plane deformation vibration. Furthermore, the peaks at 718 cm^{-1} and 530 cm^{-1} correspond to the tensile vibrations of Mn-O-Mn and Mn-O.[25] All these peaks are indicative of the molecular structure of PPy and ∝-MnO2, demonstrating the effective preparation of the ZMOP composites at a microscopic level.[26]

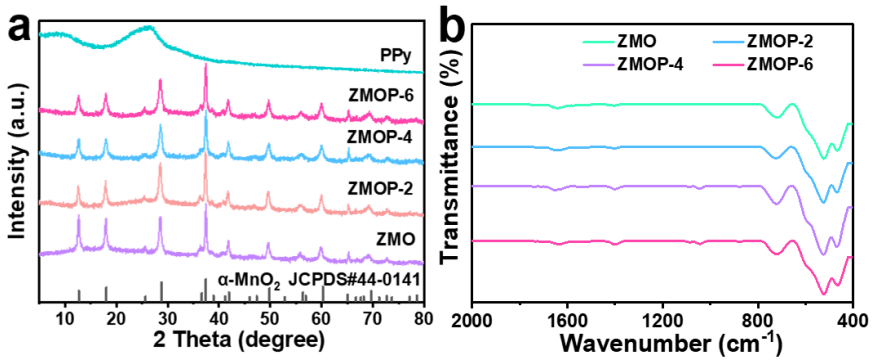

Figure 4. (a) XRD patterns of PPy、ZMO and ZMOP-x; (b) Infrared spectra of ZMO and ZMOP-x

The constituent elements and valence state of ZMOP-4 composites were further determined by XPS. As **Figure 5a** shows, the XPS full spectrum of ZMOP-4 is displayed, and it is clear that the distribution of C, N, O, Mn, Zn, and others. The contents of different elements of ZMO and ZMOP-4 are compared in **Figure 5b** . It is obvious that the content of the N element of ZMOP-4 is 1.77%, and the content of the O element is also slightly increased compared with ZMO, indicating the successful addition of PPy. In the O 1s region (in **Figure 5c)** , there are three distinct peaks at 529.9, 530.8, and 532.1 eV, which are identified as various oxygen-bonded structures: H-O-H, Mn-O-H, and Mn-O-Mn. Due to the small content of PPy, the content of the N element in ZMOP-4 is only 0.85 wt.%. During the hydrothermal reaction, the presence of nitrogen in PPy significantly enhances the electronic conductivity of the prepared electrodes. It offers active sites that reduce the band gap and boost the diffusion mechanism of Zn^{2+}, thereby contributing to the enhancement of electronic conductivity and surface capacitance (**Figure 5d**).**Figure 5e** indicates the spectra of Zn 2p, and the strong peaks at 1045.0 eV, and 1022.4 eV belong to $Zn^{2+}2p_{1/2}$ and Zn^{2+} $2p_{3/2}$, respectively. The gap between the two peaks is 22.6 eV, indicating that the valence state of Zn is +2.[27-29] **Figure 5f** shows the spectrum picture of Mn 2p. The binding energy during the Mn $2p_{3/2}$ and Mn $2p_{1/2}$ bimodal peaks is 11.5 eV, demonstrating that the main oxidation status of Mn is +3. Which is completely aligned with the reported oxidation state of MnO_2.[30] In summary, the composition and oxidation state of Mn in ZMOP-4 composites after Zn embedding can be determined, which is conducive to enhancing the stability and properties of tunneled Zn_xMnO_2. In addition, the corresponding fitting peak binding energy is slightly different from the standard value, which is attributed to the impact of Mn and N atoms.[31] By all the XPS diagrams, the ZMOP composites can be further confirmed.

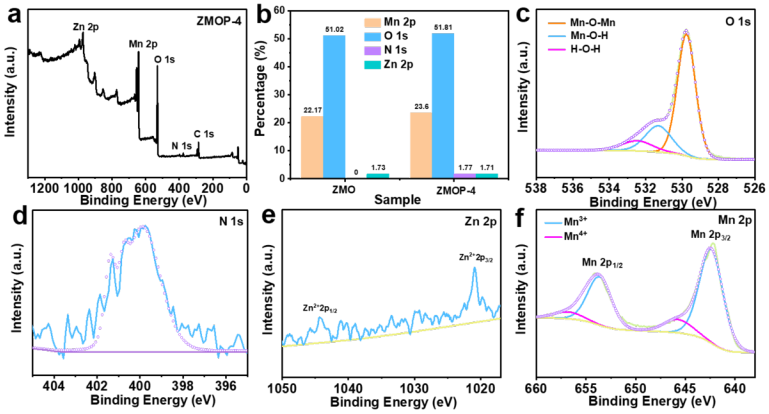

Figure 5. (a) XPS full spectra; (b) Element content comparison chart of ZMO and ZMO-4 ; High-resolution XPS spectra of (c) O 1s; (d) N 1s; (e) Zn 2p; (f) Mn 2p of ZMOP-4 sample

3.2 The Electrochemical Performance of ZMOP Cathode

To investigate the performance of ZMOP-x nanowires cathode, the Zn//ZMOP-x was assembled in the mixed aqueous solution of ZnSO4 (2 M and 0.1 M) with metal Zn anode and ZMOP-x cathode. **Figure 6a** exhibits the CV properties of Zn//ZMOP-x at different speeds (0.5, 1.0, 2.0, 3.0, 4.0, 5.0 mVs^{-1}) and the voltage window is 0.8-1.9V. It can be found that the ZMOP-4 nanowires have a pair of main redox peaks near 1.746/1.312V. The emergence of peaks could correspond to the deintercalation and intercalation of Zn^{2+} ions, which are concomitant with the oxidation and reduction reaction of the Mn +3 state. Through the rate capabilities of the ZMOP-x electrode with various PPy doping amounts, it can be found from **Figure 6b** that under different current densities, the ZMOP-4 electrode shows the best rate performance (156.4, 129.4, 84.7, 66.5, 53.2, 38.19 mAh g^{-1}). Because of the proper addition of PPy, it improves the electrical conductivity, thus accelerating the electron transfer of Zn^{2+}, so it has excellent magnification performance. The rate performance of the ZMOP-6 electrode (156.4, 129.4, 84.7, 61.5, 45.6, 29.2 mAh g^{-1}) is similar to the ZMOP-4 at low current densities region. Nevertheless, with the increasing current density, the capacity of the ZMOP-6 electrode is decreasing. Therefore, the most suitable cathode material should be ZMOP-4 nanowires. **Figure 6c** shows the EIS curves of the as-prepared materials. It was tested in the open circuit potential range of 100 kHz˜0.01 Hz. They all show low charge transfer resistance in the high-frequency region. While ZMOP-4 electrode has relatively low charge transfer resistance and a larger curve slope, indicating that the ZMOP-4 electrode has the strongest ability to rapidly diffuse ions. The pseudo-capacitance contribution of Zn//ZMOP-4 is calculated in **Figure 6d** , and the pseudo-capacitance contribution can reach 71.8% when the sweep speed reaches 5.0 mVs^{-1}. **Figure 6e** shows that ZMOP-4 nanowires exhibit outstanding cycle stability. After 5000 cycles at 0.2 A g^{-1}, the capacity retention still maintains at 82.6%, and the equivalent coulombic efficiency is 99.7%.

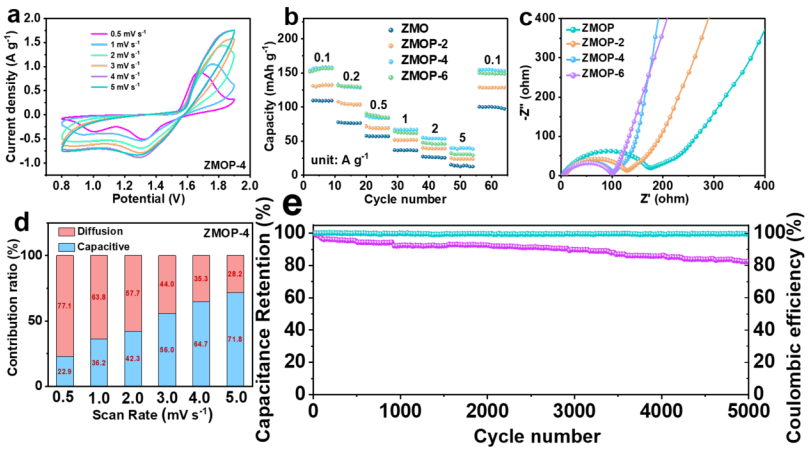

Figure 6. Electrochemical performance of Zn//ZMOP-x ZISCs: (a) CV curves at different scan rates; (b) The rate curves of Zn//ZMOP-x under different current densities; (c) Impedance comparison diagram of Zn//ZMOP-x; (d) Pseudocapacitance contribution of Zn//ZMOP-4 at different sweep speeds; (e) Performance of Zn//ZMOP-4 after 5000 cycles at 0.5 A g^{-1}

3.3 The Electrochemical Performance of ZMOP-4//PCNTs

ZISCs were assembled by ZMOP-4 cathode, PCNTs anode, and the mixed concentration $ZnSO_4$ (2 M and 0.1 M) electrolyte. The schematic diagram of ZMOP-4//PCNTs ZISCs is shown in **Figure 7a** . Meanwhile, the electrochemical properties of PCNTs anode as illustrated in **Figure S1** . **Figure S1a** shows CV curves at different sweep speeds, which are similar in shape to rectangles, indicating excellent double-layer characteristics. **Figure S1b and c** reflect the GCD data and specific capacitance curves of PCNTs at various current densities. The specific capacitance was progressively stabilized. From 0.1 A g^{-1} to 1 A g^{-1}, the specific capacitances of the PCNTs anode were 633, 306, 177.5, 140, 115, and 81.25 F g^{-1}, demonstrating the remarkable performance of the PCNTs. Furthermore, in**Figure 7b** , the CV curves of ZMOP-4 and PCNTs at the sweep speed of 1 mV s^{-1} can be seen, indicating that positive-negative electrodes both had a good response in the window range of 0-0.8 V and 0.8-1.9 V, respectively. **Figure 7c and d** show the CV curves at different sweep speeds and the GCD data of assembled ZISCs with various current densities, respectively. During the range of 0-1.9 V, the CV curves have typical redox peaks, and all curves have similar shapes at different sweep speeds. The major redox peaks at 0.56 V and 1.28 V, indicating that ZMP-4//PCNTs ZISCs have good pseudocapacitance reaction and high stability. To achieve excellent energy density of ZISCs, the mass ratio between electrodes is very important. Good linear potential time distribution can be seen through the GCD curve, which indicates good capacitance performance. Furthermore, it also indicates that the mass ratio of positive-negative electrodes is appropriate.

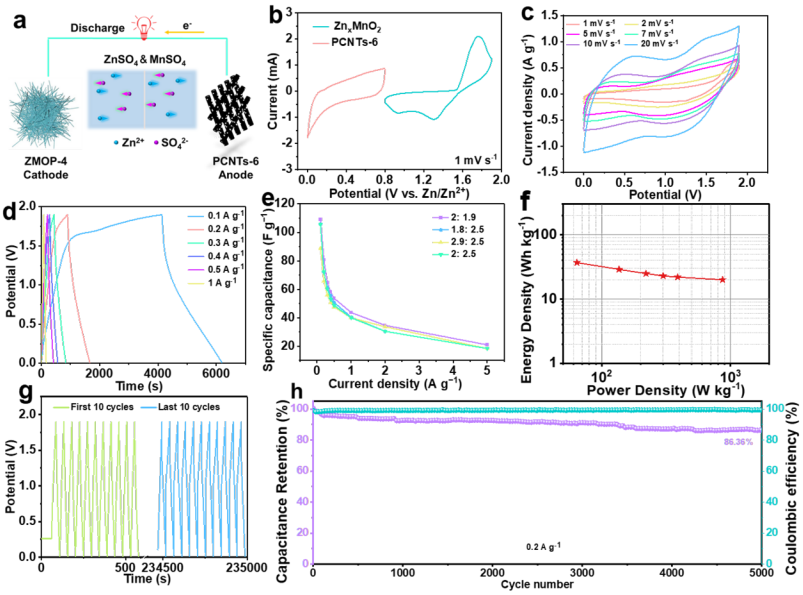

Figure 7. Electrochemical properties of PCNTs-6//ZMOP-4 ZISCs: (a) schematic diagram; (b) CV curves of Zn//Zn_xMnO_2 and Zn//PCNTs-6 at 1 mV s^{-1}; (c) CV curves of PCNTs-6//ZMOP-4 at different sweep speeds; (d) GCD curves of PCNTs-6//ZMOP-4 at different current densities; (e) specific capacitance curves with different positive and negative mass ratios; (f) energy-power density diagram; (g) GCD curves for the first 10 turns and GCD curves for the last 10 turns; (h) Zn//ZMOP-4 /PCNTs-6 cycle performance of 5000 cycles at 0.2 Ag^{-1}.

Figure 7e records the impact of different mass ratios of electrodes on the specific capacitance of assembled ZISCs. It can be seen that the different quality ratio is relatively small to the capacitance at various current densities. However, when the positive and negative quantity ratio of 2:1.9 mg, ZISCs can attain higher specific capacitance and stability. In **Figure 7f** , the ZISCs have an energy density of 37 Wh kg^{-1} at a power density of 64 W kg^{-1}. Meanwhile, when the power density is increases to 0.867 kW kg^{-1}, the energy density still maintained at 20 Wh kg^{-1}. **Figure 7g** reflects the GCD curve of 10 cycles before and after the cycle. **Figure 7h** shows that after 5000 cycles at 0.2 A g^{-1}, the device displays extraordinary cycle performance, with capacity retention of 86.36% and coulomb efficiency of 99.32%.

3.4 The Zinc-storage Mechanism of ZMOP Nanowires

To further analyze the crystal structure evolution of the ZMOP-4 cathode and the PCNTs anode during the charging-discharging procedure of ZISCs,**Figure 8a** shows the GCD curve at 2 A g^{-1}. The out-of-situ XRD results of the ZMOP-4 cathode as shown in **Figure 8b** .

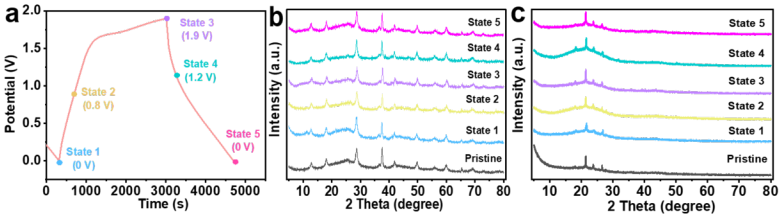

Figure 8. The reaction mechanism of Zn//ZMOP-4/PCNTs-6 ZISC is as follows: (a) GCD curve of Zn//ZMOP-4/PCNTs-6 ZISC under different charging/discharging states (current density is 0.2 A g^{-1}); (b and c) XRD patterns of ZMOP-4 cathode and PCNT-6 anode at different charging/discharging states.

The seven major characteristic peaks of the typical α-MnO_2 are distinctly described. And comparing the XRD patterns of the samples, the crystal framework of the ZMOP-4 electrode materials isn't affected by charging-discharging process can be found. The XRD pattern almost shows non-change during the charging-discharging procedure, which indicates that the tunneling crystal structure of ZMOP-4 nanowires is reversible and stable during the ion insertion/extraction process. Meanwhile, it also can support the good cyclic stability of ZISCs. Similarly, as for PCNTs anode (**Figure 8c**), there is no new crystal structure appearing, which also can indicate the excellent stability of ZISCs.

4. Conclusion

Herein, the ZMOP cathode material was fabricated by a straightforward hydrothermal method. Meanwhile, the ZISCs are successfully assembled with as-prepared materials. Comparing all the results, the ZMOP-4 cathode material exhibited the best electrochemical performance (0.1 A g^{-1}, 156.4 mAh g^{-1}). Meanwhile, with the sweep speed of 5.0 mV s^{-1}, the contribution of pseudocapacitance can exhibit 71.8%. After 5000 cycles, the capacity retention is 82.6% at 0.2 A g^{-1}. Therefore, the doping of the zinc source improved the structural stability of MnO_2. And the addition of PPy changed the structural characteristics of ZMO, greatly improving the electronic conductivity and active site. The ZISCs assembled with ZMOP-4 cathode and PCNTs anode display superb capacity (109 F g^{-1}, 0.1 A g^{-1}), and excellent power density of 867 W kg^{-1} corresponding to the energy density of 20 Wh kg^{-1}. Even after 5000 cycles, the ZISCs achieve long-cycle stability (86.4 % capacity retention, 0.2 A g^{-1}, 5000 cycles). This article offers a new perspective on the utilization of Mn-based materials and conductive polymers in ZISCs.

Acknowledgments

The Project Supported by Natural Science Basic Research Plan inShaanxi Province of China (Program No. 2024JC-YBMS-342).

Conflict of Interest

The authors declare no conflict of interest.

Data Availability Statement

The data that support the findings of this study are available in the Supporting Information material of this article.

References

1. Goodenough J B. Electrochemical energy storage in a sustainable modern society. *Energ. Environ. Sci* . 2014; 7(1): 14-18.

2. Loh K, Liew J, Liu L, et al. A comprehensive review on fundamentals and components of Zinc-ion hybrid supercapacitors. *J. Energy Storage.* 2024; 81: 110370.3. Weiss M, Ruess R, Kasnatscheew J, et al. Fast charging of lithium-ion batteries: a review of materials aspects.*Adv. Energy Mater* . 2021; 11(33): 2101126.4. Wang H, Ye W, Yang Y, et al. Zn-ion hybrid supercapacitors: achievements, challenges and future perspectives. *Nano Energy* . 2021; 85: 105942.5. Liu Y, Wu L. Recent advances of cathode materials for Zinc-ion hybrid capacitors.*Nano Energy* . 2023: 108290.6. Raza W, Ali F, Raza N, et al. Recent advancements in supercapacitor technology. *Nano Energy* . 2018; 52: 441-473.7. Lu Y, Li Z, Bai Z, et al. High energy-power Zn-ion hybrid supercapacitors enabled by layered B/N co-doped carbon cathode.*Nano Energy* . 2019; 66: 104132.8. Li H, Ma L, Han C, et al. Advanced rechargeable Zinc-based batteries: Recent progress and future perspectives. *Nano Energy* . 2019; 62: 550-587.9. He P, Chen Q, Yan M, et al. Building better Zinc-ion batteries: a materials perspective.*Energy Chem* . 2019; 1(3): 100022.10. Liu P, Liu W, Huang Y, et al. Mesoporous hollow carbon spheres boosted, integrated high performance aqueous

Zn-ion energy storage. *Energy Storage Mater* . 2020; 25: 858-865.11. Zuo S, Xu X, Ji S, et al. Cathodes for aqueous Zn-ion batteries: materials, mechanisms, and kinetics. *Chemistry-A European Journal* . 2021; 27(3): 830-860.12. Javed M, Najim T, Hussain I, et al. 2D V_2O_5 nanoflakes as a binder-free electrode material for high-performance pseudocapacitor.*Ceram. Int* . 2021; 47(17): 25152-25157.13. Ma X, Cheng J, Dong L, et al. Multivalent ion storage towards high-performance aqueous Zinc-ion hybrid supercapacitors. *Energy Storage Mater* . 2019; 20: 335-342.14. Chen Q, Jin J, Kou Z, et al. Zn^{2+}pre-intercalation stabilizes the tunnel structure of MnO_2 nanowires and enables Zinc-ion hybrid supercapacitor of battery-level energy density. *Small* . 2020; 16(14): 2000091.15. Gao F, Mei B, Xu X, et al. Rational design of $ZnMn_2O_4$ nanoparticles on carbon nanotubes for high-rate and durable aqueous Zinc-ion batteries.*Chem. Eng. J.* 2022; 448:137742.16. Wu S, Chen Y, Jiao T, et al. An aqueous Zn-ion hybrid supercapacitor with high energy density and ultrastability up to 80000 cycles. *Adv. Energy Mater.* 2019; 9(47): 1902915.17. Zhang L, Guo Y, Shen K, Huo J, Liu Y, Guo S, Ion-matching porous carbons with ultra-high surface area and superior energy storage performance for supercapacitors, *J. Mater. Chem. A* . 2019, 7: 9163–9172.18. Li H, Wu J, Wang L, Liao Q, et al. A zinc ion hybrid capacitor based on sharpened pencil-like hierarchically porous carbon derived from metal-organic framework. *Chem. Eng. J.* 2022, 428:131071.19. Zhu S, Ni J, Li Y. Carbon nanotube-based electrodes for flexible supercapacitors. *Nano Research* . 2020; 13: 1825-1841.20. Liu G, Huang H, Bi R, et al. K+ pre-intercalated manganese dioxide with enhanced Zn^{2+} diffusion for high rate and durable aqueous Zinc-ion batteries. *J. Mater. Chem. A* . 2019; 7(36): 20806-20812. 21. Wu B, Zhang G, Yan M, et al. Graphene scroll-coated α-MnO_2 nanowires as high-performance cathode materials for aqueous Zn-ion battery. *Small* . 2018; 14(13): 1703850. 22. He S, Mo Z, Shuai C, Liu W, Yue R, Liu G, Pei H, Chen Y, Liu N, Guo R. Pre-intercalation δ-MnO_2 Zinc-ion hybrid supercapacitor with high energy storage and Ultra-long cycle life. *Appl. Surf. Sci.* 2022; 577:151904.23. Liao X, Pan C, Pan Y, et al. Synthesis of three-dimensional β-MnO_2/PPy composite for high-performance cathode in zinc-ion batteries. *J. Alloy. and Compd* . 2021; 888: 161619.24. Liu Y, Chi X, Han Q, Du Y, Huang J, Liu Y, Yang J. α-MnO_2 nanofibers/carbon nanotubes hierarchically assembled microspheres: Approaching practical applications of high-performance aqueous Zn-ion batteries. *J. Power Sources.* 2019; 443:227244.25. Ng C, Lim H, Lim Y, et al. Fabrication of flexible polypyrrole/graphene oxide/manganese oxide supercapacitor. *Int. J. Energy Res* . 2015; 39(3): 344-355.26. Li Z, Huang Y, Zhang J, et al. One-step synthesis of MnO_x/PPy nanocomposite as a high-performance cathode for a rechargeable Zinc-ion battery and insight into its energy storage mechanism. *Nanoscale* . 2020; 12(6): 4150-4158.27. Wu T, Liang W. Reduced intercalation energy barrier by rich structural water in spinel $ZnMn_2O_4$ for high-rate Zinc-ion batteries. *ACS Appl. Mater. Interfaces* . 2021; 13(20): 23822-23832.28. Wu B, Zhang G, Yan M, Tong T, et al. Graphene scroll-coated α-MnO_2 nanowires as high-performance cathode materials for aqueous Zn-ion battery. *Small* . 2018 ; (13):1703850.27. Wang C, Zeng Y, Sao X, Wu S, et al. γ-MnO_2 nanorods/graphene composite as efficient cathode for advanced rechargeable aqueous zinc-ion battery. *J. Energy Chem* . 2020; 43:182-7.30. Deng X, Li J, Shan Z, et al. A N, O co-doped hierarchical carbon cathode for high-performance Zn-ion hybrid supercapacitors with enhanced pseudocapacitance. *J. Mater. Chem. A* . 2020; 8(23): 11617-11625.

31. Zang X, Wang X, Liu H, et al. Enhanced ion conduction via epitaxially polymerized two-dimensional conducting polymer for high-performance cathode in Zinc-ion batteries. *ACS Appl. Mater. Interfaces* .2020; 12(8): 9347-9354.